Monolayer CeI_2: An intrinsic room-temperature ferrovalley semiconductor

Kang Sheng,[1] Qiao Chen,[2] Hong-Kuan Yuan,[1] and Zhi-Yong Wang[1,*]
[1]*School of Physical Science and Technology, Southwest University, Chongqing 400715, China*
[2]*School of Computational Science and Electronics, Hunan Institute of Engineering, Xiangtan 411104, China*

(Received 2 January 2022; revised 27 January 2022; accepted 2 February 2022; published 14 February 2022)

Two-dimensional ferrovalley semiconductors with robust room-temperature ferromagnetism and sizable valley polarization hold great prospects for future miniature information storage devices. As a new member of the ferroic family, however, such ferrovalley materials have rarely been reported. By first-principles calculations, we identify that monolayer CeI_2 is an intrinsic ferromagnetic semiconductor and exhibits excellent ambient stability, strong easy in-plane magnetocrystalline anisotropy, and a high magnetic transition temperature up to 374 K. The ferromagnetism is found to arise from the hybridization of Ce-4f/5d and I-5p orbitals. When monolayer CeI_2 is magnetized toward the off-plane z direction, a spontaneous valley polarization as large as 208 meV in the top valence band can be achieved due to the simultaneous breaking of both inversion symmetry and time-reversal symmetry, which is further verified by the perturbation theory of spin-orbital coupling. Also, the anomalous valley Hall effect can be observed under an in-plane electrical field due to the robust valley-contrasting Berry curvature. Overall, the combination of intrinsic semiconducting ferromagnetism and spontaneous valley polarization renders monolayer CeI_2 a compelling room-temperature ferrovalley semiconductor for potential applications in nanoscale spintronics and valleytronics.

DOI: 10.1103/PhysRevB.105.075304

I. INTRODUCTION

Traditional semiconductor technology is actively dependent upon the manipulation of the carriers' charge. Nevertheless, carriers have extra degrees of freedom, such as spin and valley, which can be employed to high-efficiently encode, store, and process information [1,2]. In this regard, great breakthroughs have been made by both Xu's and Zhang's groups who experimentally observed the intrinsically ferromagnetic (FM) ordering in monolayer CrI_3 [3] and bilayer $Cr_2Ge_2Te_6$ [4] semiconductors, respectively. Unfortunately, the measured Curie temperatures in CrI_3 (45 K) and $Cr_2Ge_2Te_6$ (30 K) are far below room temperature, greatly hindering their practical applications in spintronic devices. It is thus a highly sought-after target to unveil and design 2D semiconducting materials with strong intrinsic ferromagnetism and high Curie temperature.

In analogy to charge for electronics and spin for spintronics, the valley degree of freedom,which characterizes the local energy extrema of certain valence and conduction bands, will hold great promise for the development of future valleytronic nanodevices [1,2,5–7]. Due to their large separation in the reciprocal space, such inequivalent valleys in certain crystalline materials associated with the violation of inversion symmetry can be typically robust against smooth deformations and long-wavelength phonons, eminently suitable for information processing [8–10]. Central to selectively accessing the valley states is to remove the valley degeneracy for further memory and logic operations. This has already been achieved by dynamic valley polarization based on optical pumping with circularly polarized light [11–13]. An alternative avenue to realize the valley polarization is to break time-reversal symmetry on the basis of magnetic doping [14–16], magnetic field [17–19], and magnetic proximity [20–22]. Despite these tremendous efforts to induce valley polarization in prevalent 2D 2H-phase transition metal dichalcogenides (TMDCs) through various external regulations, their applications in the field of valleytronics have been hampered due to additional difficulties and intrinsic limitations in the process of practical implementation [2,5,23]. As a consequence, it is preferable and desirable to find 2D valleytronic semiconductors beyond 2H-TMDCs yet with spontaneous valley polarization without resorting to any external modulations. Such an intriguing valley feature can be further coupled with the spin degree of freedom to make 2D ferrovalley semiconducting materials [24], which will harbor information storage and processing advantages beyond conventional charge- and spin-based semiconductor technologies, provided that the valley splitting is sufficiently large for room-temperature valleytronic applications. There are only a few theoretical reports on the intrinsic ferrovalley materials with not only a spontaneous sizable valley polarization but also a high magnetic transition temperature in the ambient environment [25–29].

In this paper, using first-principles calculations and perturbation theory, we have recognized the CeI_2 monolayer as a tantalizing room-temperature ferrovalley semiconductor where a large valley polarization can be spontaneously achieved by intrinsic ferromagnetism when the magnetic moment is along the off-plane z direction, circumventing the challenges and difficulties in the creation of extrinsic valley polarization materials. The sizable spontaneous valley polarization up to 208 meV in the top valence band of monolayer CeI_2 is attributed to the cooperative interplay between strong

*Corresponding author: zywang@swu.edu.cn

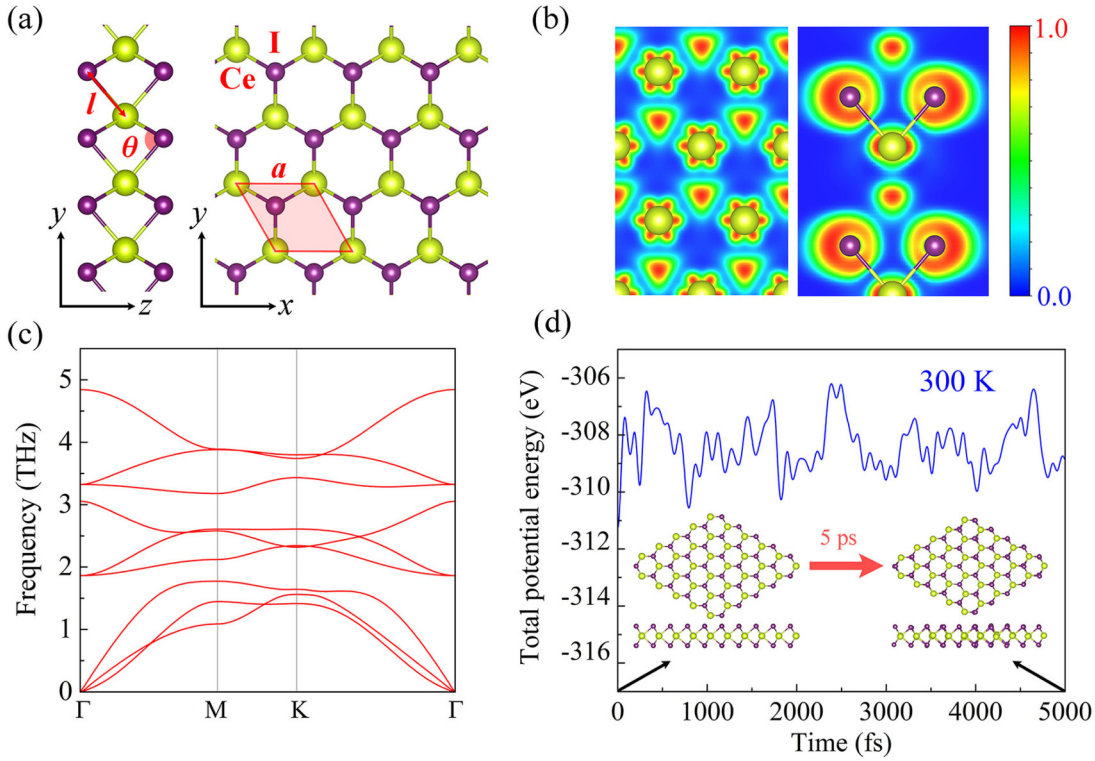

FIG. 1. (a) Side and top views of 2D CeI_2 crystal. The red shaded region denotes the unit cell. (b) Maps of the ELF over the (001) and (110) planes renormalized to values between 0.0, referring to charge depletion and 1.0 to charge accumulation. (c) Phonon dispersion spectrum of 2D CeI_2 crystal. (d) Evolution of the total energy from the 5 ps AIMD simulation at 300 K. The insets show the initial and final configurations of 2D CeI_2 crystal

magnetic exchange interaction and robust spin-orbital coupling (SOC) effect. Moreover, we confirm that the anomalous valley Hall effect (AVHE) can be realized in monolayer CeI_2 when a moderate in-plane electric field is applied. It is expected that the coexistence of spontaneous spin and valley polarizations in monolayer CeI_2 will ignite the follow-up experimental exploration.

II. COMPUTATIONAL DETAILS

Our first-principles calculations are performed by means of the density functional theory as implemented in the VIENNA AB INITIO SIMULATION PACKAGE [30,31]. The electron-ion interaction and the exchange-correlation functional are tackled, respectively, using the projector-augmented wave method [32] and the Perdew-Burke-Ernzerhof (PBE) formalism of the generalized gradient approximation [33]. The PBE + U scheme [34] in terms of both the on-site Coulomb interaction of $U = 7.470$ eV and the exchange parameter of $J = 0.989$ eV is adopted to account for the strong correction effect for the localized Ce-4f electrons [35]. Also, the more accurate Heyb-Scuseria-Ernzerhof (HSE06) hybrid functional [36] is employed to examine the obtained band structures by using the PBE + U method. An $11 \times 11 \times 1$ Γ-centered Monkhorst-Pack grid is used to sample the Brillouin zone and a vacuum region of 30 Å along the c/z direction to eliminate the image interaction between adjacent layers. The SOC effect is incorporated in the calculations of both band structure and magnetic anisotropy energy (MAE). The cutoff energy is set to 600 eV for expanding the plane-wave basis. All the structural parameters are fully relaxed until the Hellmann-Feynman force on each atom and the total energy are converged to 0.01 eV/ Å and 10^{-6} eV, respectively. A $2 \times 2 \times 1$ supercell is employed for the calculation of the phonon dispersion spectra by the PHONOPY code [37] based on the density functional perturbation theory [38]. *Ab initio* molecular dynamics (AIMD) simulation over a $5 \times 5 \times 1$ supercell is run in the canonical ensemble for 5 ps with a time step of 1.0 fs, in which the temperature is controlled at 300 K by a Nosé-Hoover thermostat [39]. Both Berry curvature and anomalous Hall conductivity are calculated by the maximally localized Wannier functions (MLWFs) as encoded in the WANNIER90 package [40].

III. RESULTS AND DISCUSSION

The crystal structure of monolayer CeI_2 is shown in Fig. 1(a), which exhibits a 2D hexagonal lattice with the $P\bar{6}m2$ space group. The central Ce atom is coordinated by six neighboring I atoms in a trigonal prismatic geometry, and then the Ce atomic layer is sandwiched by two I atomic layers. In analogy to monolayers 2H-GdX_2 (X = F, Cl, Br, and I) [26,41], the inversion symmetry is broken in monolayer CeI_2. The lattice constant, the Ce-I bond length, and the Ce-I-Ce bond angle are optimized at the PBE + U level to $a = 4.28$ Å, $l = 3.25$ Å, and $\theta = 82.37°$, respectively. Moreover, we calculate the electron localization function (ELF) in the (001) and (110) planes to elucidate the bonding character in CeI_2. As shown

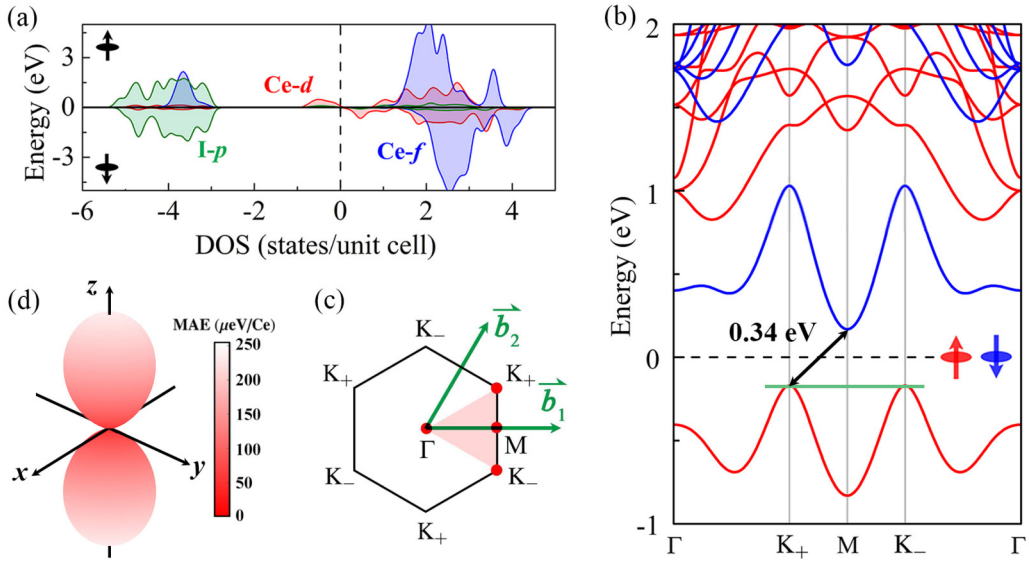

FIG. 2. (a) Orbital-resolved DOS and (b) spin-resolved band structure at the PBE + U level without the involvement of the SOC effect for 2D CeI_2 crystal in the FM ground state. The Fermi level is set as energy zero. (c) Schematic diagram of the 2D first Brillouin zone with high-symmetry points. (d) Magnetic anisotropy of 2D CeI_2 crystal. The MAE is set to zero in the xy plane.

in Fig. 1(a), electrons are mainly located around the Ce and I atoms, and almost no electrons are localized at the center region between them, indicative of a typical ionic bonding nature with electrons being transferred from the Ce to I atoms. This bond character agrees with the large difference in the electronegativity between the bonded atoms.

To evaluate the stability of monolayer CeI_2, we first calculate the cohesive energy, which is defined as $E_{coh} = (E_{Ce} + 2E_I - E_{CeI_2})/3$. Here E_{Ce} and E_I are the energies of single isolated Ce and I atoms, while E_{CeI_2} is the total energy of 2D CeI_2 unit cell. The calculated E_{coh} is 3.14 eV per atom. This value is comparable to those of experimentally synthesized 2D materials such as Cu_2Ge (3.17 eV per atom) [42] and phosphorene (3.48 eV per atom) [43], implying that it is possible to fabricate CeI_2 in the laboratory. Also, we compute the formation energy by $E_{form} = (\mu_{Ce} + 2\mu_I - E_{CeI_2})/3$, where μ_{Ce} and μ_I are the energies per Ce and I atoms in their most stable bulk structures, respectively. The resultant E_{form} is 1.36 eV per atom, demonstrating the preference of monolayer CeI_2 formation rather than the pure Ce and I phases.

Then we investigate the phonon dispersion spectrum of monolayer CeI_2. As shown in Fig. 1(c), the absence of imaginary modes across the entire Brillouin zone confirms its dynamical stability. Furthermore, an AIMD simulation is implemented for 5 ps at the temperature of 300 K. It is found from Fig. 1(d) that the total energy shows little fluctuation and the crystal structure displays no evident disruption during the entire simulation, demonstrating robust thermal stability for monolayer CeI_2 at room temperature. In addition, we calculate the elastic constants of monolayer CeI_2. For 2D hexagonal systems, the elastic constants form a symmetric 6×6 tensor matrix in the linear elastic range [44], which are calculated to be $C_{11} = C_{22} = 31.52$ N/m, $C_{12} = 10.40$ N/m, and $C_{44} = 10.56$ N/m, respectively. These values satisfy the Born-Huang criteria of mechanical stability [45,46], namely, $C_{11}, C_{44} > 0$ and $C_{11}C_{22} - C_{12}^2 > 0$. In brief, all of these calculations jointly verify that monolayer CeI_2 harbors excellent structural stability for the freestanding form in the ambient environment.

Figure 2(b) displays the spin-resolved band structure of monolayer CeI_2 in the absence of the SOC effect by the PBE + U method. As seen, monolayer CeI_2 is a 2D intrinsic FM semiconductor with an indirect band gap of 0.34 eV and a pair of energetically degenerate valleys at the K_+ and K_- high-symmetry points of the Brillouin zone in the valence band. The intrinsic spin polarization breaks the time-reversal symmetry of $E_\uparrow(K_+) = E_\downarrow(K_-)$, where the arrows refer to the spin directions. Also, monolayer CeI_2 has another pair of additional valleys in the second-lowest unoccupied conduction band. It is noted that the two pairs of degenerate valleys are inequivalent due to the violation of inversion symmetry by the D_{3h} crystal symmetry, making monolayer CeI_2 a valleytronic semiconductor. Since the valence and conduction bands come from opposite spin channels when approaching the Fermi level, monolayer CeI_2 is also a typical bipolar magnetic semiconductor (BMS) [47,48]. Its conduction band minimum and valence band maximum reside at the M and K points of 2D Brillouin zone, respectively. As shown in Figs. S1 and S2 of the Supplemental Material (SM) [49], both the bottom conduction and top valence bands consist of the Ce-5$d_{x^2-y^2}$, Ce-5d_{xy}, and Ce-5d_{z^2} orbitals with a minor contribution from the I-5p_z orbital. In spite of the localization around different k-regions, the Ce-5$d_{x^2-y^2}$ and Ce-5d_{xy} orbitals are degenerate in energy and establish strong hybridization with the Ce-5d_{z^2} and I-5p_z orbitals. For such a BMS material, the unique electronic structure enables the feasibility to achieve half-metallicity by applying an appropriate gate voltage [50], which can provide 100% spin-polarized current for high-efficiency spintronic devices. In addition, the calculations based on the HSE06 functional are also carried out

for comparison. It is found from Figs. S3 of the SM [49] that apart from a large band gap of 0.98 eV, the HSE06 scheme reveals the same electronic feature as obtained by the PBE + U computations. In consideration of computational cost, we will make use of the PBE + U method for all calculations in the following discussion.

Next, we concentrate on the magnetic properties of CeI_2 based on the optimized structure. To determine the magnetic ground state, we take two collinear magnetic configurations into account in a $2 \times 2 \times 1$ supercell, which cover one FM state and one antiferromagnetic (AFM) state, as shown in Fig. S4 of the SM [49]. It is found that the FM configuration is energetically lower than the stripy AFM one by 48.29 meV per Ce atom, indicating that CeI_2 prefers the FM coupling. The preference of the FM state is closely related to the geometric structure of monolayer CeI_2, in which the Ce–I–Ce bond angle is estimated to be 82.37°, close to 90.00°. In light of the Goodenough-Kanamori-Anderson rules [51–53], such a structure will favor the FM coupling due to the superexchange interaction between the neighboring Ce atoms mediated by the I atom. In consideration of the fact that the valence electronic configuration is $4f^15d^16s^2$ of an isolated Ce atom, there will be two electrons transferred from one Ce atom to the six neighboring I atoms when forming monolayer CeI_2, yielding Ce^{2+} with an electronic state of $4f^15d^16s^0$. As a consequence, the half-filled $4f_{x(x^2-3y^2)}$ and $5d_{z^2}$ orbitals give rise to a formal magnetic moment of $2\mu_B$ on each Ce atom, see Fig. S2 in the SM [49]. Also, our DFT calculations confirm that CeI_2 exhibits a spontaneous spin-polarized state with a magnetic moment of $2\mu_B$ per unit cell. Figure S4 in the SM presents the spin density distribution [49] that manifests the magnetism in the FM ground state, which is predominantly contributed by the Ce atoms. From Fig. 2(a), the asymmetric distribution of the density of states (DOS) below the Fermi level further sheds light on the ferromagnetism of monolayer CeI_2. At the microscopic level, the DOS reveals that the magnetism in CeI_2 comes from the Ce-4f and Ce-5d orbital electrons as well as the I-5p orbital electrons. The occupied Ce-4f states significantly hybridize with the I-5p states at around 3.65 eV below the Fermi level, and there is also a weak Ce-5d/I-5p hybridization state in the top valence band. In this regard, our observation is partially different from monolayers 2H-GdX_2 (X = F, Cl, Br, and I) [26,54] where the Gd-4f orbitals are highly localized without any involvement of hybridization with the I-5p orbitals.

According to the Mermin-Wagner theorem [55], the long-range FM ordering in low-dimensional systems may be easily destroyed at finite temperatures by strong thermal fluctuations. However, the discovery of 2D magnetic CrI_3 [3] and $Cr_2Ge_2Te_6$ [4] semiconductors unveils that magnetic anisotropy scaled by MAE, which arises mainly from the SOC effect, plays a crucial role in the magnetic ordering stability. It is now understood that the larger the MAE, the stronger the resistance of magnetic ordering against the thermal fluctuations, and thus the better the performance for data storage [48,56]. The MAE is defined as the energy difference MAE = $E_{\text{off-plane}} - E_{\text{in-plane}}$ between the off-plane and in-plane magnetization directions by incorporating the SOC effect. The positive or negative MAE characterizes that the easy magnetization axis is in-plane or off-plane orientation.

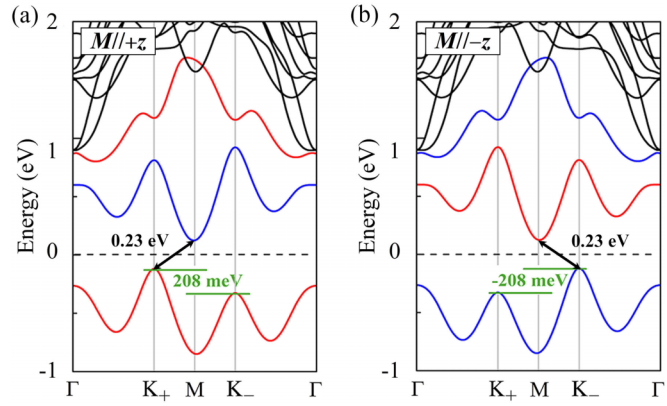

FIG. 3. The SOC band structure at the PBE + U level with the (a) positive and (b) negative magnetic moments for 2D CeI_2 crystal in the FM ground state. The red and blue lines near the Fermi level set as zero energy refer to the spin-up and spin-down states, respectively.

Figure 2(d) displays the MAE of monolayer CeI_2 through the whole space. It is observed that the MAE is strongly dependent on the magnetization direction in the xz and yz planes, while the MAE is isotropic in the xy plane of the CeI_2 monolayer. In particular, the MAE is zero in the layer plane and reaches a maximum of 234 μeV per Ce atom normal to the plane, comparable to those of monolayers CrXTe$_3$ (X = Si, Ge, and Sn) (209, 110, and 69 μeV per Cr atom) [57] and sufficiently large to counterbalance the thermal fluctuations and thus make CeI_2 suitable for magnetoelectronic applications. Similar to 2D VSi_2N_4 [58] and GdI_2 [59] crystals, monolayer CeI_2 exhibits an easy magnetization plane, such that there is no energetic barrier to the rotation of magnetization in the xy plane. For this reason, this system can be considered as a 2D XY magnet. As we will show below, the magnetization can be adjusted from the in-plane to off-plane direction through overcoming an energy barrier of 234 μeV, which can then lead to the occurrence of a sizable valley polarization.

To explore the potential applications in spintronics of monolayer CeI_2 working at ambient environment, the Curie temperature or a more generic magnetic transition temperature should be comparable to or above the room temperature. For a 2D XY magnet with a typical triangle lattice structure, Monte Carlo simulations have shown that a Berezinskii-Kosterlitz-Thouless magnetic transition to a quasi-long-range phase could take place at a critical temperature $T_C = 1.335\ J/k_B$ [25,60], where $J = (E_{AFM} - E_{FM})/8S^2$ is the nearest-neighboring exchange parameter and k_B is the Boltzmann constant. With $E_{AFM} - E_{FM} = 193.16$ meV in a $2 \times 2 \times 1$ supercell and $S = 1$, T_C is estimated to be 374 K. It should be noted that if the J value is calculated by means of the HSE06 hybrid functional, the obtained T_C will be higher [29,54]. Overall, the combination of sizable MAE and intrinsic FM ordering above room-temperature renders monolayer CeI_2 a promising candidate for future high efficiency spintronic applications [54,59,61].

Figure 3 displays the SOC band structure of monolayer CeI_2 with the magnetization along the $\pm z$ directions, respectively. Apart from the decrease of indirect band gap from 0.34

to 0.23 eV, the incorporation of the SOC effect removes the energetic degeneracy of the K_+ and K_- valleys in the top valence band, resulting in an intriguing valley polarization. The valley energy difference between the K_+ and K_- valleys is found to depend on the magnetization direction. If the magnetization is oriented toward the $+z$ direction, the valley polarization from the spin-up channel reaches up to 208 meV. Such a sizable valley polarization is sufficiently robust against the thermal noise for logic operations at room-temperature [5,62], which is equivalent to that of a valley degenerate material exposed to an external magnetic field of around $1040 \sim 2080$ Tesla [17]. Once reversing the magnetization to the $-z$ direction, the K_- valley becomes higher than the K_+ valley in energy, establishing a valley polarization of -208 meV in the spin-down channel. In other words, the spin and valley polarization can be flipped concurrently by reversing the magnetic moment of Ce atoms, which provides an efficient avenue to tailor the valley properties of monolayer CeI_2 by regulating its orientation of magnetization. Moreover, there is no trivial band within the transport energy window from -1 to 0 eV, superior to those situations in which the valley polarization is created by using typical extrinsic approaches [11–16]. The feature indicates minimal interference from the other states of Brillouin zone to the valley performance of monolayer CeI_2. These findings in combination with the high T_C above room-temperature can establish the robust spin-valley coupling and thus make monolayer CeI_2 an ideal ferrovalley material for practical applications in nonvolatile data storage, valley filter, and valley valve as well as other spintronic and valleytronic devices [24].

The underlying physics for the valley polarization in monolayer CeI_2 can be ascribed to the cooperative interplay between intrinsic ferromagnetism and strong SOC effect. In the absence of the SOC effect, Fig. 2(b) demonstrates that the magnetic exchange coupling yields a significant spin splitting between the spin-up and spin-down bands due to the time-reversal symmetry breaking, but both K_+ and K_- valleys in the valence band from the same spin channel remain degenerate in energy. In the nonmagnetic state, on the other hand, Fig. S5 in the SM [49] indicates that the SOC effect splits the spin degeneracy at the K_+ and K_- valleys due to the violation of inversion symmetry. However, the time-reversal symmetry makes two valleys from opposite spin channels energetically degenerate. Consequently, only when considering both magnetic exchange coupling and robust SOC effect together, the K_+ and K_- valleys of monolayer CeI_2 would no longer be degenerate in energy, giving rise to the significant spontaneous valley polarization.

Also, one can see from Fig. 3 that the K_+ and K_- valleys in the second-lowest unoccupied conduction band remain energetically close to each other, in sharp contrast to the sizable valley polarization in the top valence band. The discrepancy can be interpreted in terms of the orbitals' contribution to the band edges of monolayer CeI_2. According to Fig. S2 of the SM [49], the valleys in the valence band arise from the Ce-$5d_{x^2-y^2}$ and Ce-$5d_{xy}$ orbitals, while the valleys in the conduction band from the Ce-$5d_{z^2}$ orbital. Since the ferromagnetism of monolayer CeI_2 breaks spin degeneracy between the spin-up and spin-down bands, the SOC Hamiltonian only involves the interaction of the same spin states, which can be approximately written as [28,58,63,64]

$$\hat{H}_{\mathrm{SOC}} = \lambda \hat{S}_{z'}(\hat{L}_z \cos\theta + \tfrac{1}{2}\hat{L}_+ e^{-i\phi}\sin\theta + \tfrac{1}{2}\hat{L}_- e^{+i\phi}\sin\theta), \tag{1}$$

where λ refers to the SOC-related constant, as well as $\hat{S}_{z'}$ and $\hat{L}_z$ to the z'/z components of spin and orbital angular momenta, respectively. Both $\theta \in [0, \pi)$ and $\phi \in [0, 2\pi)$ define the spin orientation, which are corresponding to the polar and azimuthal angles, respectively, $\hat{L}_+ = \hat{L}_x + i\hat{L}_y$ and $\hat{L}_- = \hat{L}_x - i\hat{L}_y$. When the magnetization is along the $+z$ direction ($\theta = 0$), Eq. (1) can be further simplified as $\hat{H}_{\mathrm{SOC}} = \lambda \hat{S}_{z'}\hat{L}_z = \alpha \hat{L}_z$. In consideration of the orbitals' contribution and the wave vector symmetry at the K_+ and K_- valleys, the basis functions are chosen as $|\psi_{\mathrm{c}}^{\tau}\rangle = |d_{z^2}\rangle$ and $|\psi_{\mathrm{v}}^{\tau}\rangle = \frac{1}{\sqrt{2}}(|d_{x^2-y^2}\rangle + i\tau|d_{xy}\rangle)$, where $\tau = \pm 1$ refers to the valley index and c/v to the conduction and valence bands. The energy levels at the K_+ and K_- valleys are then defined as $E_{\mathrm{c}}^{\tau} = \langle\psi_{\mathrm{c}}^{\tau}|\hat{H}_{\mathrm{SOC}}|\psi_{\mathrm{c}}^{\tau}\rangle$ and $E_{\mathrm{v}}^{\tau} = \langle\psi_{\mathrm{v}}^{\tau}|\hat{H}_{\mathrm{SOC}}|\psi_{\mathrm{v}}^{\tau}\rangle$, respectively. Accordingly, the valley polarizations in the second-lowest energy conduction band and the top valence band are given by

$$E_{\mathrm{c}}^{+} - E_{\mathrm{c}}^{-} = 0, \tag{2}$$

$$E_{\mathrm{v}}^{+} - E_{\mathrm{v}}^{-} = i\langle d_{x^2-y^2}|\hat{H}_{\mathrm{SOC}}|d_{xy}\rangle - i\langle d_{xy}|\hat{H}_{\mathrm{SOC}}|d_{x^2-y^2}\rangle = 4\alpha, \tag{3}$$

respectively. Here, we have made use of $\hat{L}_z|d_{x^2-y^2}\rangle = 2i|d_{xy}\rangle$ and $\hat{L}_z|d_{xy}\rangle = -2i|d_{x^2-y^2}\rangle$. Similarly, when the magnetization is along the $-z$ direction ($\theta = \pi$), one can readily obtain $E_{\mathrm{c}}^{+} - E_{\mathrm{c}}^{-} = 0$ and $E_{\mathrm{v}}^{+} - E_{\mathrm{v}}^{-} = -4\alpha$. Clearly, these results agree with the difference of the valley polarizations in the conduction and valence bands of monolayer CeI_2 from first-principles calculations.

Arising from the simultaneous breaking of both both inversion symmetry and time-reversal symmetry in a 2D hexagonal system, it is well-known that the nonzero Berry curvatures at the K_+ and K_- valleys are required to be not only opposite in sign but also different in magnitude along the off-plane direction. To confirm the valley-contrasting physics in monolayer CeI_2, we calculate its Berry curvature along the z direction for the nth band at a given $\mathbf{k}$ state, which can be expressed as a summation over all the occupied states [65],

$$\boldsymbol{\Omega}_z(\mathbf{k}) = -\sum_n \sum_{n\neq m} f_n(\mathbf{k}) \frac{2\mathrm{Im}\langle\psi_{n\mathbf{k}}|\hat{v}_x|\psi_{m\mathbf{k}}\rangle\langle\psi_{m\mathbf{k}}|\hat{v}_y|\psi_{n\mathbf{k}}\rangle}{(E_{n\mathbf{k}} - E_{m\mathbf{k}})^2}, \tag{4}$$

where $f_n(\mathbf{k})$ is the Fermi-Dirac distribution function, $\hat{v}_x$ is the x component of velocity operator, and $E_{n\mathbf{k}}$ is the eigenvalue of Bloch wave function $\psi_{n\mathbf{k}}$. By integrating the Berry curvature over the 2D Brillouin zone, the anomalous Hall conductivity reads [28,66]

$$\sigma_{xy} = -\frac{e^2}{\hbar}\int_{BZ} \frac{d\mathbf{k}}{(2\pi)^2}\boldsymbol{\Omega}_z(\mathbf{k}). \tag{5}$$

To guarantee the quality of the MLWFs in the calculation of both Berry curvature and anomalous Hall conductivity, Fig. S6 of the SM [49] shows the SOC band structure of monolayer CeI_2 on the basis of the Wannier functions, which is found to match well with the band dispersion near the Fermi level obtained by the PBE + U method. This comparison

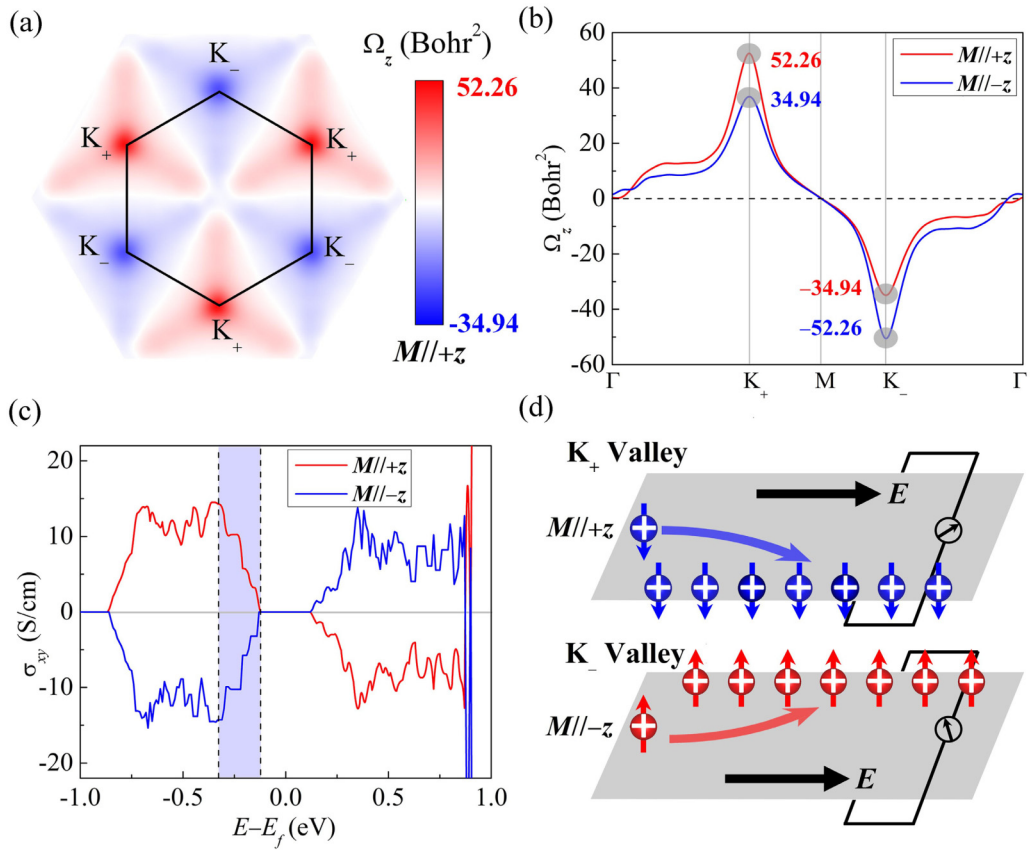

FIG. 4. Berry curvature of 2D CeI_2 crystal (a) over the 2D Brillouin zone and (b) along the high-symmetry lines. (c) Anomalous Hall conductivity as a function of the eigenvalue $E_{n\mathbf{k}}$. Two vertical dashed lines denote the two valley extrema in the top valence band. (d) Schematic AVHEs for the hole-doped CeI_2 monolayer at the K_+ and K_- valleys under the action of an in-plane electric field. The red and blue arrows stand for the spin-up and spin-down states, respectively.

verifies that the constructed Wannier functions are sufficiently localized.

Figure 4(a) presents the calculated Berry curvature of monolayer CeI_2 as a contour map over the whole 2D Brillion zone. As expected, $\mathbf{\Omega}_z(K_+) = 52.26$ Bohr^2 and $\mathbf{\Omega}_z(K_-) = -34.94$ Bohr^2 have opposite signs and unequal magnitudes, indicating a robust valley-contrasting Berry curvature in monolayer CeI_2. It is necessary to stress that once reversing the magnetization from the $+z$ to $-z$ direction, the magnitudes of Berry curvature at the K_+ and K_- valleys exchange to each other but their signs remain unchanged. As shown in Fig. 4(b), the $\mathbf{\Omega}_z(K_+)/\mathbf{\Omega}_z(K_-)$ is still positive/negative but becomes $34.94/-52.26$ Bohr^2 when the spins are all flipped. Under the action of an in-plane electric field, the nonzero Berry curvature can serve as an effective magnetic field, endowing the Bloch electrons with an anomalous transverse velocities $v_\perp \sim \boldsymbol{E} \times \mathbf{\Omega}_z(\mathbf{k})$ [67]. Because of the valley polarization, the energies of the two valleys are different. A careful hole doping can adjust the Fermi level to fall between the K_+ and K_- valleys, which makes the doped holes reside in one valley. As a consequence, the valley-contrasting Berry curvature forces the hole carriers to accumulate on one side of the sample upon applying an in-plane electric field, giving rise to an AVHE in monolayer CeI_2. As illustrated in Fig. 4(d), when such p-type CeI_2 is magnetized toward the $+z$ direction, the positive Berry curvature drives the spin-down holes from the K_+ valley to accumulate on the right side of the sample in the presence of an in-plane electric field. Once the magnetization is reversed, the spin-up holes from the K_- valley transfer to the left side of the sample due to the action of negative Berry curvature. Apart from the AVHE, it is also interesting to note from Fig. 4(d) that the charge and spin Hall effects occur in monolayer CeI_2, which can be more readily detected in experiments. To demonstrate this, we further calculate the anomalous Hall conductivity. As seen from Fig. 4(c), a valley-polarized σ_{xy} is achieved when the Fermi level is located between the energies of two valleys in the top valence band, regardless of the orientation of magnetization. The resultant Hall voltage along the transversal direction can be measured simply by a voltmeter at hand, facilitating the observation of AVHE and the practical valleytronic applications.

IV. CONCLUSION

In conclusion, we identify that monolayer CeI_2 is an intrinsic room-temperature ferrovalley semiconductor via first-principles calculations. As a stable 2D XY ferromagnet on one hand, it exhibits not only easy in-plane magnetocrystalline anisotropy with a sizable MAE of 234 μeV but also a high magnetic transition temperature of 374 K. Intrinsic ferromagnetism in monolayer CeI_2 is ascribed to the hybridization

between the Ce-$4f/5d$ and I-$5p$ orbitals. As a promising 2D valleytronic semiconductor on the other hand, when the magnetization is oriented toward the off-plane z direction, a spontaneous valley polarization up to 208 meV is observed in the top valence band of monolayer CeI_2 due to the combination of the ferromagnetism and the SOC effect and further validated by a perturbation theory. Also, its valley-contrasting Berry curvature provides an effective avenue to selectively steer the valley states. These outstanding features make monolayer CeI_2 have great potential in fabricating spintronic and valleytronic nanodevices working at room-temperature.

ACKNOWLEDGMENTS

This research was sponsored by the National Natural Science Foundation of China under Grant No. 11774041, the Fundamental Research Funds for the Central Universities under Grant No. SWU019021, and Chongqing Key Laboratory of Micro-Nano Structure Optoelectronics.

The authors declare no competing financial interests. K.S. and Z.-Y.W. conceptualized the work and analyzed the data, K.S. performed the research, Q.C. made the formal analysis, H.-K.Y. provided the VASP software, and Z.-Y.W. supervised the project and wrote the paper.

[1] J. R. Schaibley, H. Yu, G. Clark, P. Rivera, J. S. Ross, K. L. Seyler, W. Yao, and X. Xu, Nat. Rev. Mater. **1**, 16055 (2016).
[2] S. Zhao, X. Li, B. Dong, H. Wang, H. Wang, Y. Zhang, Z. Han, and H. Zhang, Rep. Prog. Phys. **84**, 026401 (2021).
[3] B. Huang, G. Clark, E. Navarro-Moratalla, D. R. Klein, R. Cheng, K. L. Seyler, D. Zhong, E. Schmidgall, M. A. McGuire, D. H. Cobden, W. Yao, D. Xiao, P. Jarillo-Herrero, and X. Xu, Nature (London) **546**, 270 (2017).
[4] C. Gong, L. Li, Z. Li, H. Ji, A. Stern, Y. Xia, T. Cao, W. Bao, C. Wang, Y. Wang, Z. Qiu, R. Cava, S. G. Louie, J. Xia, and X. Zhang, Nature (London) **546**, 265 (2017).
[5] S. A. Vitale, D. Nezich, J. O. Varghese, P. Kim, N. Gedik, P. Jarillo-Herrero, D. Xiao, and M. Rothschild, Small **14**, 1801483 (2018).
[6] G. Scuri, T. I. Andersen, Y. Zhou, D. S. Wild, J. Sung, R. J. Gelly, D. Bérubé, H. Heo, L. Shao, A. Y. Joe, A. M. Mier Valdivia, T. Taniguchi, K. Watanabe, M. Lončar, P. Kim, M. D. Lukin, and H. Park, Phys. Rev. Lett. **124**, 217403 (2020).
[7] Y. Liu, Y. Gao, S. Zhang, J. He, J. Yu, and Z. Liu, Nano Res. **12**, 2695 (2019).
[8] O. L. Sanchez, D. Ovchinnikov, S. Misra, A. Allain, and A. Kis, Nano Lett. **16**, 5792 (2016).
[9] L. Xu, M. Yang, L. Shen, J. Zhou, T. Zhu, and Y. P. Feng, Phys. Rev. B **97**, 041405(R) (2018).
[10] H. Z. Lu, W. Yao, D. Xiao, and S. Q. Shen, Phys. Rev. Lett. **110**, 016806 (2013).
[11] H. Zeng, J. Dai, W. Yao, D. Xiao, and X. Cui, Nat. Nanotechnol. **7**, 490 (2012).
[12] K. F. Mak, K. He, J. Shan, and T. F. Heinz, Nat. Nanotechnol. **7**, 494 (2012).
[13] T. Cao, G. Wang, W. Han, H. Ye, C. Zhu, J. Shi, Q. Niu, P. Tan, E. Wang, B. Liu, and J. Feng, Nat. Commun. **3**, 887 (2012).
[14] Y. C. Cheng, Q. Y. Zhang, and U. Schwingenschlögl, Phys. Rev. B **89**, 155429 (2014).
[15] R. Peng, Y. Ma, S. Zhang, B. Huang, and Y. Dai, J. Phys. Chem. Lett. **9**, 3612 (2018).
[16] X. Chen, L. Zhong, X. Li, and J. Qi, Nanoscale **9**, 2188 (2017).
[17] D. MacNeill, C. Heikes, K. F. Mak, Z. Anderson, A. Kormányos, V. Zólyomi, J. Park, and D. C. Ralph, Phys. Rev. Lett. **114**, 037401 (2015).
[18] X.-X. Zhang, T. Cao, Z. Lu, Y.-C. Lin, F. Zhang, Y. Wang, Z. Li, J. C. Hone, J. A. Robinson, D. Smirnov, S. G. Louie, and T. F. Heinz, Nat. Nanotechnol. **12**, 883 (2017).
[19] A. Srivastava, M. Sidler, A. V. Allain, D. S. Lembke, A. Kis, and A. Imamoğlu, Nat. Phys. **11**, 141 (2015).
[20] C. Zhao, T. Norden, P. Zhang, P. Zhao, Y. Cheng, F. Sun, J. P. Parry, P. Taheri, J. Wang, Y. Yang, T. Scrace, K. Kang, S. Yang, G. Miao, R. Sabirianov, G. Kioseoglou, W. Huang, A. Petrou, and H. Zeng, Nat. Nanotechnol. **12**, 757 (2017).
[21] B. Zhou, Z. Li, J. Wang, X. Niu, and C. Luan, Nanoscale **11**, 13567 (2019).
[22] Q. Zhang, S. A. Yang, W. Mi, Y. Cheng, and U. Schwingenschlögl, Adv. Mater. **28**, 959 (2016).
[23] H. Guan, N. Tang, H. Huang, X. Zhang, M. Su, X. Liu, L. Liao, W. Ge, and B. Shen, ACS Nano **13**, 9325 (2019).
[24] W.-Y. Tong, S.-J. Gong, X. Wan, and C.-G. Duan, Nat. Commun. **7**, 13612 (2016).
[25] P. Jiang, L. Kang, Y.-L. Li, X. Zheng, Z. Zeng, and S. Sanvito, Phys. Rev. B **104**, 035430 (2021).
[26] H.-X. Cheng, J. Zhou, W. Ji, Y.-N. Zhang, and Y.-P. Feng, Phys. Rev. B **103**, 125121 (2021).
[27] C. Luo, X. Peng, J. Qu, and J. Zhong, Phys. Rev. B **101**, 245416 (2020).
[28] R. Li, J. Jiang, W. Mi, and H. Bai, Nanoscale **13**, 14807 (2021).
[29] C. Zhang, Y. Nie, S. Sanvito, and A. Du, Nano Lett. **19**, 1366 (2019).
[30] G. Kresse and J. Furthmüller, Phys. Rev. B **54**, 11169 (1996).
[31] G. Kresse and J. Furthmüller, Comput. Mater. Sci. **6**, 15 (1996).
[32] P. E. Blöchl, Phys. Rev. B **50**, 17953 (1994).
[33] J. P. Perdew, K. Burke, and M. Ernzerhof, Phys. Rev. Lett. **77**, 3865 (1996).
[34] A. I. Liechtenstein, V. I. Anisimov, and J. Zaanen, Phys. Rev. B **52**, R5467 (1995).
[35] P. Larson, W. R. L. Lambrecht, A. Chantis, and M. van Schilfgaarde, Phys. Rev. B **75**, 045114 (2007).
[36] J. Heyd, G. E. Scuseria, and M. Ernzerhof, J. Chem. Phys. **118**, 8207 (2003).
[37] A. Togo and I. Tanaka, Scr. Mater. **108**, 1 (2015).
[38] S. Baroni, S. de Gironcoli, A. Dal Corso, and P. Giannozzi, Rev. Mod. Phys. **73**, 515 (2001).
[39] D. Bucher, L. C. T. Pierce, J. A. McCammon, and P. R. L. Markwick, J. Chem. Theory Comput. **7**, 890 (2011).
[40] N. Marzari, A. A. Mostofi, J. R. Yates, I. Souza, and D. Vanderbilt, Rev. Mod. Phys. **84**, 1419 (2012).
[41] K. Sheng, H.-K. Yuan, and Z.-Y. Wang, Phys. Chem. Chem. Phys. **24**, 3865 (2022).

[42] L. M. Yang, I. A. Popov, A. I. Boldyrev, T. Heine, T. Frauenheim, and E. Ganz, Phys. Chem. Chem. Phys. **17**, 17545 (2015).
[43] V. Vierimaa, A. V. Krasheninnikov, and H.-P. Komsa, Nanoscale **8**, 7949 (2016).
[44] E. Cadelano, P. L. Palla, S. Giordano, and L. Colombo, Phys. Rev. B **82**, 235414 (2010).
[45] M. Born and K. Huang, *Dynamical Theory of Crystal Lattices* (Clarendon, Oxford, 1954).
[46] Z.-j. Wu, E.-j. Zhao, H.-p. Xiang, X.-f. Hao, X.-j. Liu, and J. Meng, Phys. Rev. B **76**, 054115 (2007).
[47] X. Li, X. Wu, Z. Li, J. Yang, and J. G. Hou, Nanoscale **4**, 5680 (2012).
[48] Y. Wu, W. Sun, S. Liu, B. Wang, C. Liu, H. Yin, and Z. Cheng, Nanoscale **13**, 16564 (2021).
[49] See Supplemental Material at http://link.aps.org/supplemental/10.1103/PhysRevB.105.075304 for more details of monolayer CeI_2.
[50] X. Li and J. Yang, Phys. Chem. Chem. Phys. **15**, 15793 (2013).
[51] B. Goodenough, Phys. Rev. **100**, 564 (1955).
[52] J. Kanamori, J. Phys. Chem. Solids **10**, 87 (1959).
[53] P. W. Anderson, Phys. Rev. **115**, 2 (1959).
[54] K. Sheng, H.-K. Yuan, and Z.-Y. Wang, J. Mater. Chem. C **9**, 16495 (2021).
[55] N. D. Mermin and H. Wagner, Phys. Rev. Lett. **17**, 1133 (1966).
[56] K. Sheng, Z.-Y. Wang, H.-K. Yuan, and H. Chen, New J. Phys. **22**, 103049 (2020).
[57] H. L. Zhuang, Y. Xie, P. R. C. Kent, and P. Ganesh, Phys. Rev. B **92**, 035407 (2015).
[58] Q. Cui, Y. Zhu, J. Liang, P. Cui, and H. Yang, Phys. Rev. B **103**, 085421 (2021).
[59] B. Wang, X. Zhang, Y. Zhang, S. Yuan, Y. Guo, S. Dong, and J. Wang, Mater. Horiz. **7**, 1623 (2020).
[60] S. Zhang, R. Xu, W. Duan, and X. Zou, Adv. Funct. Mater. **29**, 1808380 (2019).
[61] Y. Guo, S. Zhou, and J. Zhao, J. Mater. Chem. C **9**, 6103 (2021).
[62] T. Norden, C. Zhao, P. Zhang, R. Sabirianov, A. Petrou, and H. Zeng, Nat. Commun. **10**, 4163 (2019).
[63] R. Peng, Y. Ma, X. Xu, Z. He, B. Huang, and Y. Dai, Phys. Rev. B **102**, 035412 (2020).
[64] M.-H. Whangbo, E. E. Gordon, H. Xiang, H.-J. Koo, and C. Lee, Acc. Chem. Res. **48**, 3080 (2015).
[65] D. J. Thouless, M. Kohmoto, M. P. Nightingale, and M. den Nijs, Phys. Rev. Lett. **49**, 405 (1982).
[66] T. Cai, S. A. Yang, X. Li, F. Zhang, J. Shi, W. Yao, and Q. Niu, Phys. Rev. B **88**, 115140 (2013).
[67] D. Xiao, M. C. Chang, and Q. Niu, Rev. Mod. Phys. **82**, 1959 (2010).